Molecular Dynamics Simulation of Heat Transfer and Phase Change During Laser Material Interaction

Xinwei Wang

Xianfan Xu
e-mail: xxu@ecn.purdue.edu

School of Mechanical Engineering,
Purdue University,
West Lafayette, IN 47907

In this work, heat transfer and phase change of an argon crystal irradiated by a picosecond pulsed laser are investigated using molecular dynamics simulations. The result reveals no clear interface when phase change occurs, but a transition region where the crystal structure and the liquid structure co-exist. Superheating is observed during the melting and vaporizing processes. The solid-liquid interface is found to move with a velocity of hundreds of meters per second, and the vapor is ejected from the surface with a vapor front velocity of hundreds of meters per second. [DOI: 10.1115/1.1445289]

Introduction

In recent years, ultrashort pulsed lasers have been rapidly developed and employed in materials processing. Due to the extremely short pulse duration, many difficulties exist in experimental investigation of laser material interaction, such as measuring the transient surface temperature, the velocity of the solid-liquid interface, and the material ablation rate. Ultrashort laser material interaction involves several coupled, nonlinear, and non-equilibrium processes inducing an extremely high heating rate (10^{16} K/s) and a high temperature gradient (10^{11} K/m). The continuum approach of solving the heat transfer problem becomes questionable under these extreme situations. In contrast, molecular dynamics (MD) simulation, which analyzes the movement of atoms or molecules directly, is suitable for investigating the ultrashort laser material interaction process. One aim of this work is to use MD simulation to investigate heat transfer occurring in ultrashort laser-material interaction and compares the results with those obtained with the continuum approach.

A large amount of work has been dedicated to studying laser material interaction using MD simulations. Due to the limitation of computer resources, most work was restricted to systems with a small number of atoms, thus only qualitative results such as the structural change due to heating were obtained. For instance, using quantum MD simulations, Shibahara and Kotake studied the interaction between metallic atoms and the laser beam in a system consisting of 13 atoms or less [1,2]. Their work was focused on the structural change of metallic atoms due to laser beam absorption. Häkkinen and Landman [3] studied dynamics of superheating, melting, and annealing at the Cu surface induced by laser beam irradiation using the two-step heat transfer model developed by Anisimov et al. [4]. This model describes the laser metal interaction in two steps including photon energy absorption in electrons and lattice heating through interaction with electrons. Several works in the literature investigated laser-induced ablation in various systems. Kotake and Kuroki [5] studied laser ablation of a small dielectric system consisting of 4851 atoms. Laser beam absorption was simulated by exciting the potential energy of atoms. Applying the same laser beam absorption approach, Herrmann and Campbell [6] investigated laser ablation of a silicon crystal containing approximately 23,000 atoms. Zhigileit et al. [7,8] stud-

ied laser induced ablation of organic solids using the breathing sphere model, which simulated laser irradiation by vibrational excitation of molecules. Because of the arbitrary properties chosen in the calculation, their calculation results were qualitative, and were restricted to systems with tens of thousands of atoms. Ohmura et al. [9] attempted to study laser metal interaction with the MD simulation using the Morse potential function for metals [10]. The Morse potential function simplified the potential calculation among the lattice and enabled the study of a larger system with 160,000 atoms. Heat conduction by the electron gas, which dominates heat transfer in metals, could not be predicted by the Morse potential function. Alternatively, heat conduction was simulated using the finite difference method based on the thermal conductivity of metal. Laser material interaction in a larger system was recently investigated by Etcheverry and Mesaros [11]. In their work, a crystal argon solid containing about half a million atoms was simulated. For laser induced acoustic waves, a good agreement between the MD simulation and the numerical thermoelastic calculation was obtained.

In this work, MD simulations are conducted to study laser argon interaction. The system under study has 486,000 atoms, which makes it possible to study the effect of volumetric absorption of laser energy, to define and track the solid/liquid and liquid/vapor interfaces, and to investigate whether the system is in thermal equilibrium. The number of the atoms is chosen as a compromise between the simulation accuracy and the computational time. Laser energy absorption is implemented as an increase in the kinetic energy of atoms. Laser heating of argon with different laser fluences is investigated. Laser induced heat transfer, melting, and vaporization are emphasized in this work. Phase change relevant parameters, such as the velocity of solid-liquid and liquid-vapor interfaces, ablation rate, and ablation threshold fluence are reported.

Theory of MD Simulation

In this work, argon is chosen as the material to be studied because of the physically meaningful Lennard-Jones (LJ) 12-6 potential and the less computational time required. The basic problem involves solving Newtonian equations for each atom interacting with its neighbors by means of a pairwise Lennard-Jones force:

$$m_i \frac{d^2 r_i}{dt^2} = \sum_{j \neq i} F_{ij}, \qquad (1)$$

where m_i and r_i are the mass and position of atom i, respectively, F_{ij} is the force between atoms i and j, which is obtained from the Lennard-Jones potential as $F_{ij} = -\partial\phi_{ij}/\partial r_{ij}$. The Lennard-Jones potential ϕ_{ij} is expressed as

$$\phi_{ij} = 4\varepsilon\left[\left(\frac{\sigma}{r_{ij}}\right)^{12} - \left(\frac{\sigma}{r_{ij}}\right)^{6}\right], \tag{2}$$

where ε is the LJ well depth parameter, σ is the equilibrium separation parameter, and $r_{ij} = r_i - r_j$.

Many different algorithms have been developed to solve Eqs. (1) and (2), of which the Verlet algorithm is widely used due to its numerical stability, convenience, and simplicity [12]. In this calculation, the half-step leap-frog scheme is used, which is a modification to the velocity Verlet algorithm and is expressed as [12]

$$v(t+\delta t/2) = v(t-\delta t/2) + \frac{F_{ij}(t+\delta t)}{m_i}\delta t \tag{3a}$$

$$r_i(t+\delta t) = r_i(t) + v(t+\delta t/2)\delta t \tag{3b}$$

$$F_{ij}(t+\delta t) = -\frac{\partial\phi_{ij}(t+\delta t)}{\partial r_{ij}} \tag{3c}$$

$$v(t) = \frac{1}{2}(v(t+\delta t/2) + v(t-\delta t/2)). \tag{3d}$$

The criterion for choosing δt is that it should be much smaller than the typical time taken for an atom to travel its own length [12]. In this work, δt is taken as 25 fs, much smaller than the typical time (850 fs) for an argon atom to travel its own length. The distance between atoms is first compared with a potential cutoff distance r_c. Only when the distance is less than r_c is the force calculated. In this calculation, r_c is taken as 2.5σ, which is widely adopted in MD simulations using the LJ potential. At this distance, the potential is only about 1.6 percent of the well depth. The comparison of the atomic distance with r_c is organized using the cell structure and linked list method [12].

Laser energy absorption in the material is treated by scaling the velocities of all atoms in each structural cell by an appropriate factor. The amount of energy deposited in each cell is calculated assuming the laser beam is exponentially absorbed in the target. In order to prevent undesired amplification of atomic macromotion, the average velocity of atoms in each layer of the structural cells is subtracted before the velocity scaling. This laser energy absorption model de-emphasizes the details of laser material interaction, in which the quantum mechanical effect needs to be accounted for. However, the time scale for the process of laser energy absorption ($\sim$1 ps) is much smaller than the time scale considered in this work. Therefore, without knowing the details of the laser material interaction, the thermal effect can still be investigated using the current absorption model.

Results of Calculation

The target studied consists of 90 fcc unit cells in x and y directions, and 15 fcc unit cells in the z direction. Each unit cell contains 4 atoms, and the system consists of 486,000 atoms. In both x and y directions, the computational domain has a size of 48.73 nm. In the z direction, the size of the computational domain is 17.14 nm with the bottom of the target located at 4.51 nm and the top surface (the laser irradiated surface) at 12.63 nm. The schematic of the computational domain is shown in Fig. 1. The values of the parameters used in the calculation are listed in Table 1.

Thermal Equilibrium Calculation. The first step in the calculation is to initialize the system so that it is in thermal equilibrium with a minimum potential energy before laser heating. This is achieved by a thermal equilibrium calculation. Periodical boundary conditions are assumed on the surfaces in x and y directions, and free boundary conditions on the surfaces in the z direction. The target is initially constructed based on the fcc lattice
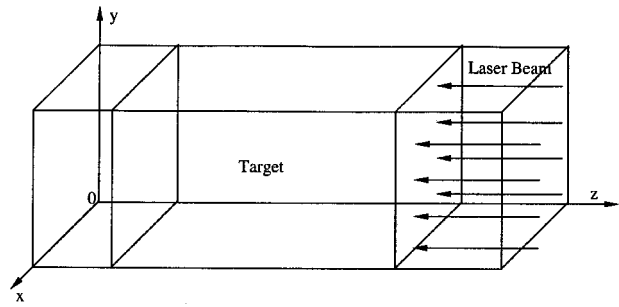

Fig. 1 Scheme of the computational domain.

structure with the (100) surface facing up. The nearest neighbor distance, r_s in the fcc lattice of argon depends on temperature T, and is initialized using the expression given by Broughton and Gilmer [13],

$$\frac{r_s}{\sigma}(T) = 1.0964 + 0.054792\left(\frac{k_B T}{\varepsilon}\right) + 0.014743\left(\frac{k_B T}{\varepsilon}\right)^2$$
$$+ 0.083484\left(\frac{k_B T}{\varepsilon}\right)^3 - 0.23653\left(\frac{k_B T}{\varepsilon}\right)^4 + 0.25057\left(\frac{k_B T}{\varepsilon}\right)^5. \tag{4}$$

Initial velocities of atoms are specified randomly from a Gaussian distribution based on the specified temperature of 50 K using the following formula,

$$\frac{1}{2}m\sum_{i=1}^{3}v_i^2 = \frac{3}{2}k_B T, \tag{5}$$

where k_B is the Boltzmann constant. During the equilibrium calculation, due to the variation of the atomic positions, the temperature of the target may change because of the exchange between the kinetic and potential energies. In order to allow the target to reach thermal equilibrium at the expected temperature, velocity scaling is necessary to adjust the temperature of the target during the early period of equilibrium. The velocity scaling approach proposed by Berendsen et al. [14] is applied in this work. At each time step, velocities are scaled by a factor χ expressed as:

$$\chi = \left(1 + \frac{\delta t}{t_T}\left(\frac{T}{\xi}\right)\right)^{1/2}, \tag{6}$$

Table 1 Values of the parameters used in the calculation

Parameter	Value
ε, LJ well depth parameter	1.653×10^{-21} J
σ, LJ equilibrium separation	0.3406 nm
m, Argon atomic mass	66.3×10^{-27} kg
k_B, Boltzmann constant	1.38×10^{-23} J/K
a, Lattice constant	0.5414 nm
r_c, Cut off distance	0.8515 nm
Size of the sample $-x$	48.726 nm
Size of the sample $-y$	48.726 nm
Size of the sample $-z$	8.121 nm
Time step	25 fs
Number of atoms	486000

where ξ is the current kinetic temperature, and t_T is a preset time constant, which is taken as 0.4 ps. This technique forces the system towards the desired temperature at a rate determined by t_T, while only slightly perturbing the forces on each atom. After scaling the velocity for 50 ps, the average temperature of the system reaches the desired value. Then the calculation is continued for another 100 ps to improve the uniformity of temperature in the target. The final equilibrium temperature of the target is 49.87 K, which is close to the desired temperature of 50 K.

At thermal equilibrium, the atomic velocity distribution should follow the Maxwellian distribution

$$P_M = 4 \pi v^2 \left(\frac{m}{2 \pi k_B T} \right)^{3/2} e^{-mv^2/2k_B T}, \tag{7}$$

where P_M is the probability for an atom moving with a velocity v. The velocity distribution based on the simulation results and the Maxwellian distribution are shown in Fig. 2, which indicates a good agreement between the two.

Figure 3 shows the lattice structure in the x-z plane when the system is in thermal equilibrium. For the purpose of illustration, only the atoms in the range of $0 < x < 12$ nm and $0 < y < 12.6$ nm are plotted. It is seen that atoms are located around their equilibrium positions, and the lattice structure is preserved. Another observation is that at the top and the bottom surfaces of the target, a few atoms have escaped due to the free boundary conditions.

In order to check the validity of the MD model, the thermal physical properties of argon are calculated and compared with published data. The specific heat at constant pressure (vacuum), the specific heat at constant volume, and the thermal conductivity
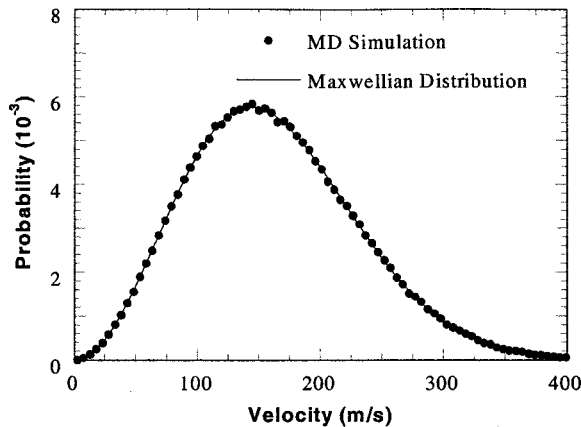

Fig. 2 Comparison of the velocity distribution by the MD simulation with the Maxwellian velocity distribution.
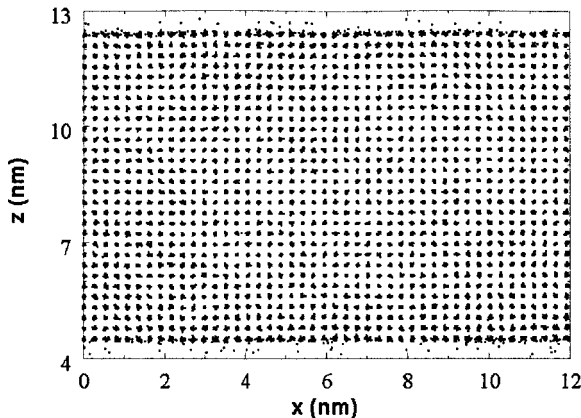

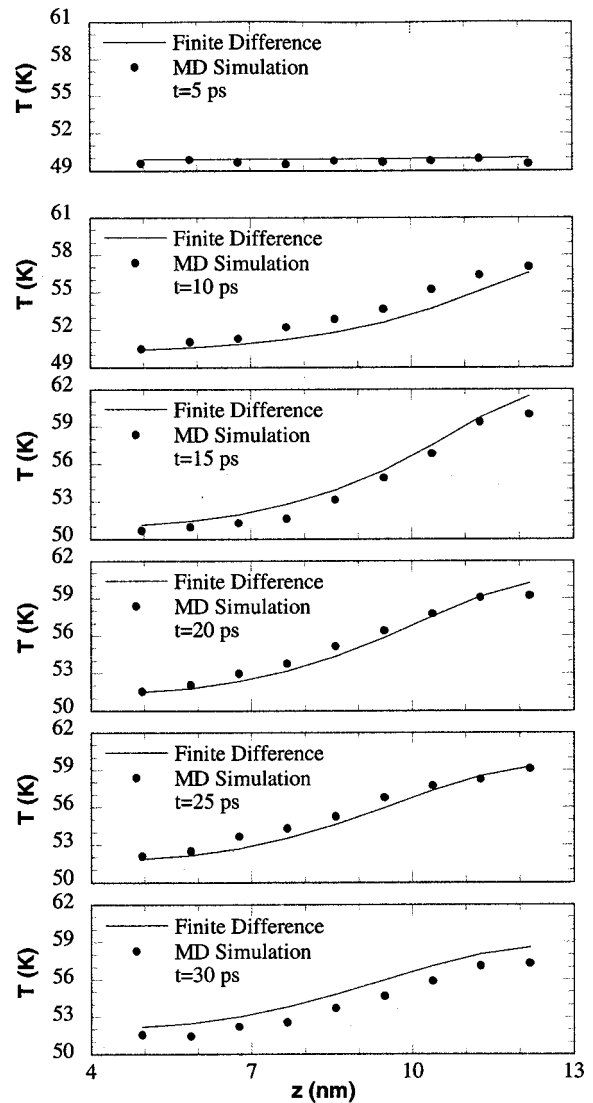Fig. 3 Structure of the target in the x-z plane within the range of 0<x<12 nm and 0<y<12.6 nm.

Fig. 4 Temperature distribution in the target illuminated with a laser pulse of 0.06 J/m².

are calculated to be 787.8 J/kg·K, 576.0 J/kg·K, and 0.304 W/m·K, while the experimental data are 637.5 J/kg·K, 543.5 J/kg·K, and 0.468 W/m·K, respectively [15]. The difference between the MD simulation results and the experimental data arises from the free boundary conditions used in MD simulations whereas the experiments were conducted under the atmospheric pressure.

Laser Material Interaction. In calculating the laser material interaction, periodical boundary conditions are used on the surfaces in x and y directions, and free boundary conditions on the surfaces in the z direction. The simulation corresponds to the problem of irradiating a block of argon in vacuum. The laser beam is uniform in space, and has a temporal Gaussian distribution with a 5 ps FWHM centered at 10 ps. The laser beam energy is absorbed exponentially in the target and is expressed as

$$\frac{dI}{dz} = -I(z)/\tau, \tag{8}$$

where I is the laser beam intensity, and τ is the characteristic absorption depth. The experimental value of τ is not available, but is expected to be intensity dependent. In the calculation, τ is chosen to be 2.5 nm.
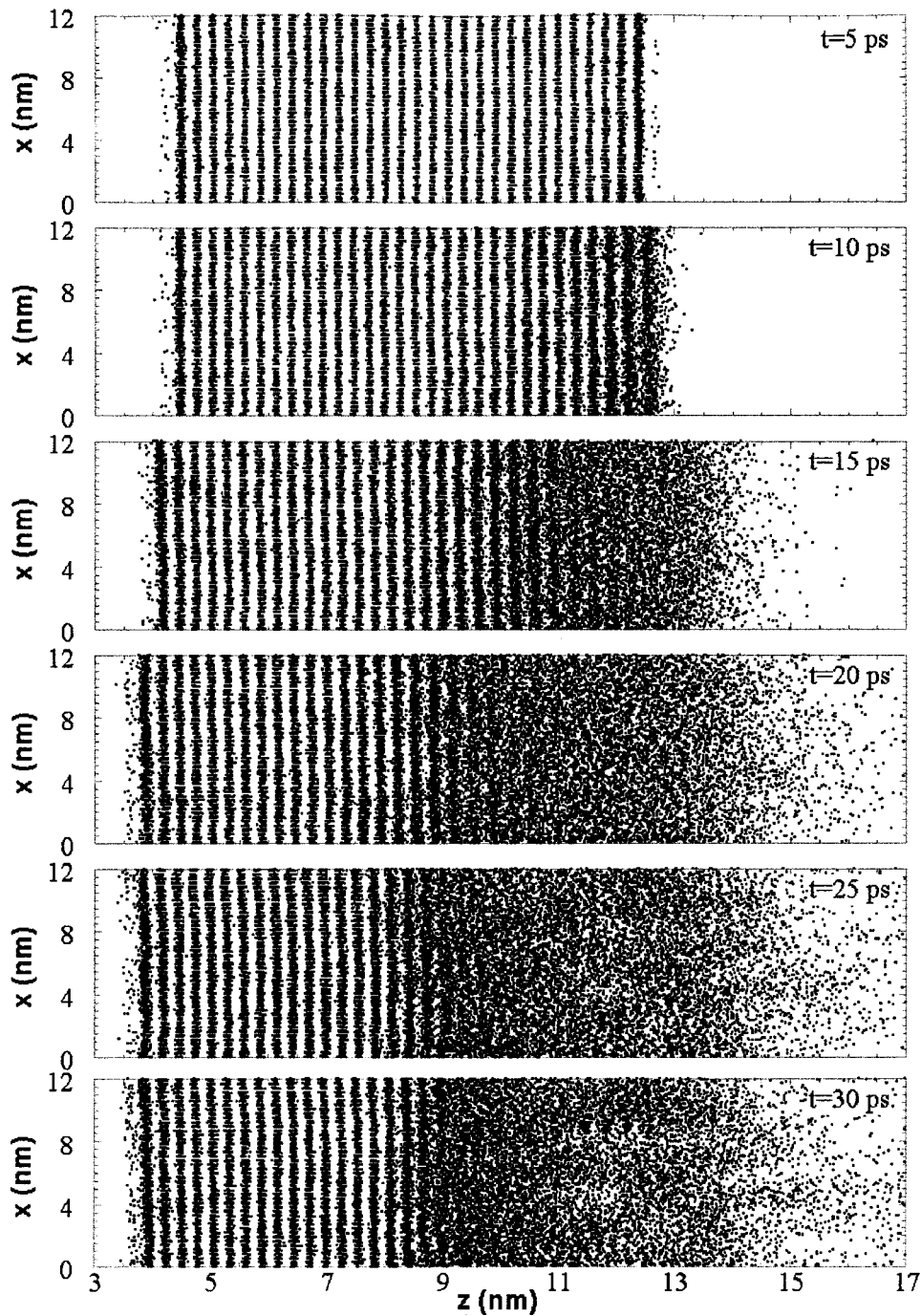
Fig. 5 Snapshots of atomic positions in argon illuminated with a laser pulse with a fluence of 0.7 J/m².

Laser Heating. The temperature distribution in the target illuminated with a laser pulse of 0.06 J/m² is first calculated and compared with the results from a finite difference calculation. No phase change occurs at this laser fluence. Figure 4 shows the temperature distribution calculated using the MD simulation and the finite difference method. In the MD simulation, the temperature at different locations is calculated as an ensemble average of a domain with a thickness of 2.5σ in the z direction. In the finite difference calculation, properties of argon obtained with the MD simulation are used in order to study the validity of the continuum approach in ps laser materials interaction, i.e., heating is very intense and localized and the temperature gradient is extremely high. It can be seen from Fig. 4 that the results obtained from the

MD simulation are close to those obtained by the finite difference method. The difference between them is on the same order of the statistical uncertainty of the MD simulation. In other words, the continuum approach is still capable of predicting the heating process induced by a picosecond laser pulse. It is also noticed that no thermal wave is obtained in the MD simulation, therefore the non-Fourier effect [16] is insignificant. However, the thermal relaxation time of argon at the temperature range studied in this work is small ($\sim$1 ps). The non-Fourier effect would not be observed using the continuum approach either.

Laser Induced Phase Change. In this section, various phenomena accompanying phase change in an argon target illumi-
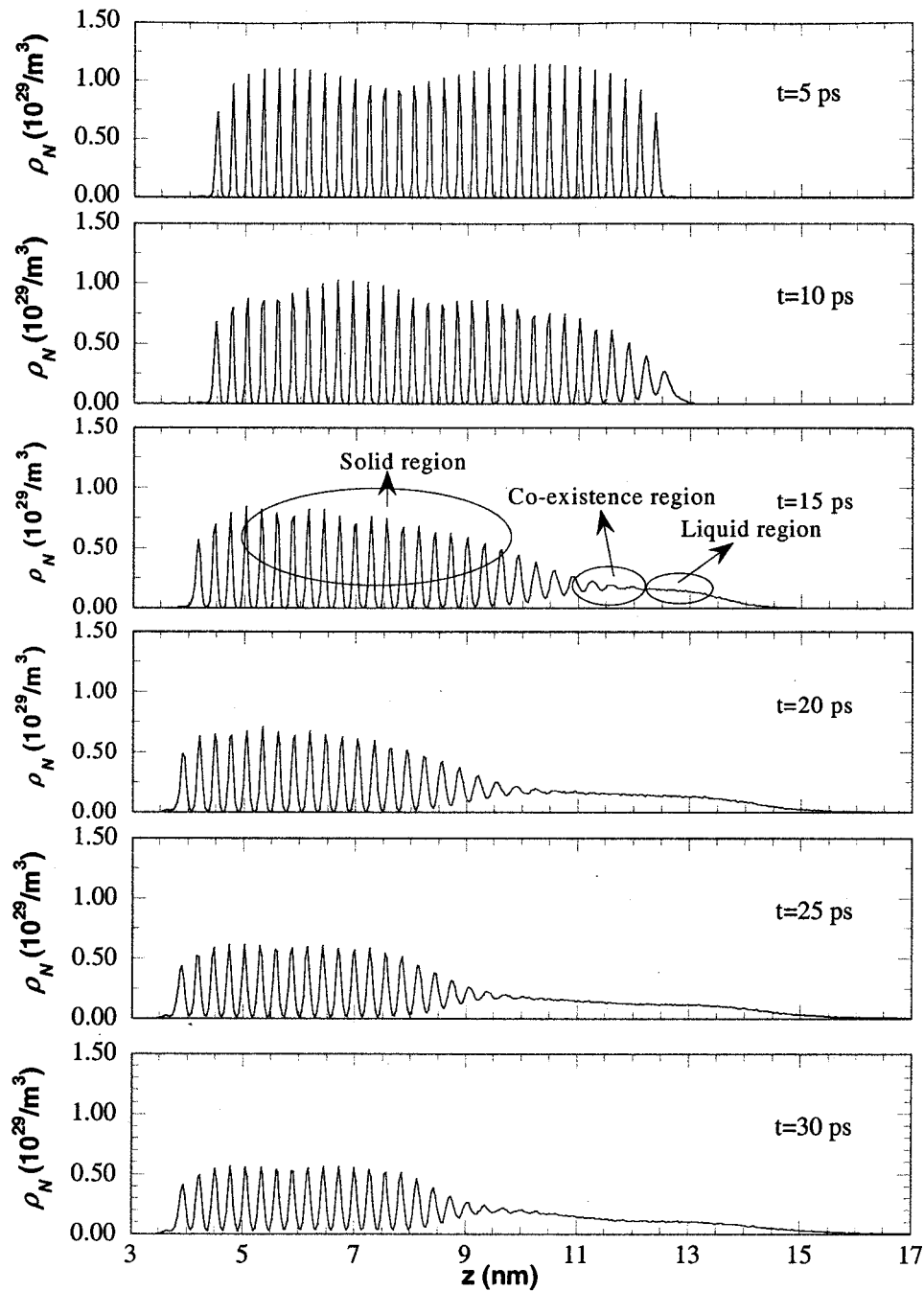
Fig. 6 Distribution of the number density of atoms at different times in argon illuminated with a laser pulse of 0.7 J/m².

nated with a laser pulse of 0.7 J/m² are investigated in detail. The threshold fluence for ablation is also studied. Towards the end of the laser pulse, the laser beam absorption is considered in both the solid and non-solid parts. The laser beam absorption depth is adjusted based on the local material density ρ_{local}, and is calculated as $\tau\rho/\rho_{local}$, with ρ denoting the density of the solid before laser heating.

A series of snapshots of atomic positions at different times is shown in Fig. 5. It is seen that until 10 ps, the lattice structure is preserved in the target. At about 10 ps, melting starts, and the lattice structure is destroyed in the melted region and is replaced by a random atomic distribution. After 20 ps, the solid liquid interface stops moving into the target, and vaporized atoms are clearly seen. Figure 6 shows the spatial distribution of the number

density of atoms, ρ_N, at different times, which further illustrates the structural change during laser heating. At the early stage of laser heating, the crystal structure is preserved in the target, which is seen as the peak number density of atoms at each lattice layer. Due to the increase of atomic kinetic energy in laser heating, atoms vibrate more intensely in the solid region, resulting in a lower peak of the number density of atoms and a wider distribution. As laser heating progresses, the target is melted from its front surface, and the atomic distribution becomes random. Therefore, the number density of atoms becomes uniform over the melted region. However, no clear interface is observed between the solid and the liquid. Instead, structures of solid and liquid co-exist within a certain range, which is shown as the co-existence of the peak and the high base of the number density of atoms. Vaporiza-

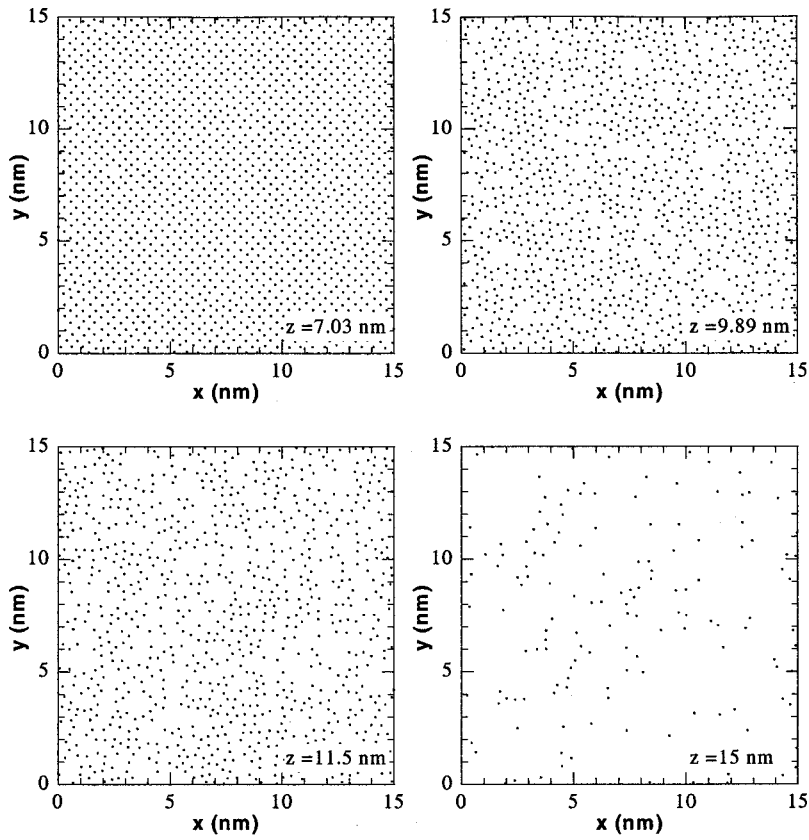Journal of Heat Transfer

APRIL 2002, Vol. 124 / **269**

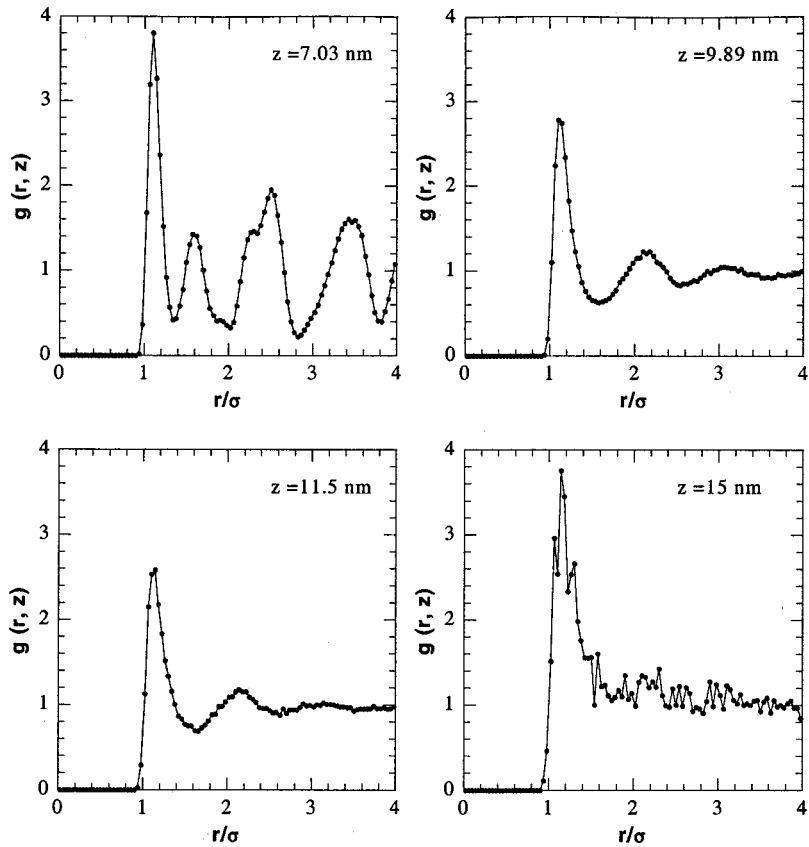Fig. 7 In-plane structures reflected by the atomic positions at different z locations at 20 ps.

Fig. 8 In-plane radial distribution functions at different z locations at 20 ps.
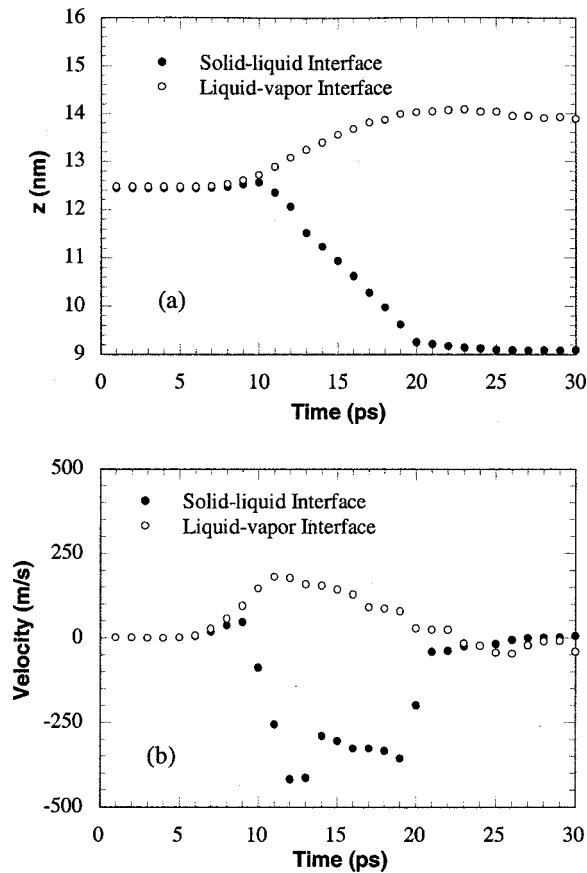
Fig. 9 (*a*) **Positions, and** (*b*) **velocities of the solid-liquid interface and the liquid-vapor interface in argon illuminated with a laser pulse of 0.7 J/m².**
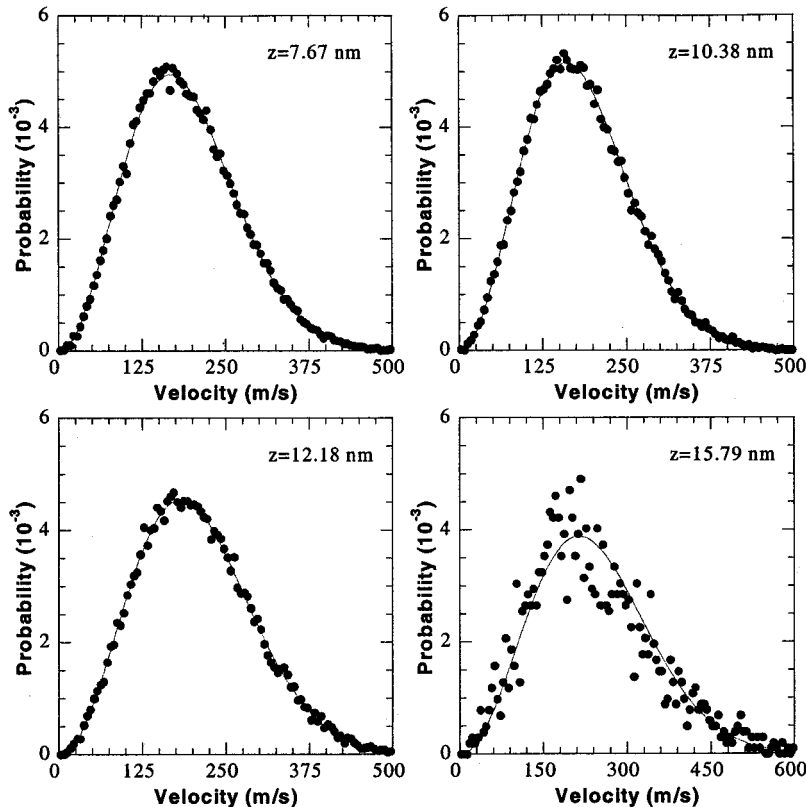
tion happens at the surface of the target, which reduces the number density of atoms significantly at the location near the liquid surface.

In addition to the structure variation in the z direction as discussed above, the in-plane structure also reflects the phase change process. Figure 7 shows the atomic positions within a 0.27 nm thick plane centered at various z locations at 20 ps. For the purpose of illustration, only the area within $0 < x < 15$ nm and $0 < y < 15$ nm is plotted. In the solid region ($z = 7.03$ nm), atoms are located regularly in space, reflecting the crystal lattice structure. In the transient region ($z = 9.89$ nm), the lattice structure still can be found in small localized regions while the whole atomic distribution looks random. A similar structure is found in the liquid region ($z = 11.5$ nm). However, localized regions with the short order structure are much fewer than those at $z = 9.89$ nm. In the vapor region ($z = 15$ nm), fewer atoms are found with no apparent structures.

One of the parameters describing the in-plane structure is the in-plane radial distribution function $g(r)$ [12,17,18]. It is a ratio of the number of atoms at a distance r from a given atom compared with the number of atoms at the same distance in an ideal gas with the same density. Figure 8 shows $g(r,z)$ in the same planes discussed in Fig. 7. From Fig. 8, structures of different phases can be quantified. At the location of 7.03 nm, both the short-range and long-range orders are preserved, showing the feature of the crystalline structure. At the location of 9.89 nm, the short-range order (the second peak) still exists while the long-range order becomes much less apparent, showing the co-existence of the solid and the liquid. At 11.5 nm, the material only has a short-range order, reflecting a liquid-like structure. The short-range order disappears at the location of 15 nm, indicating a gas-like structure.

In order to find out the rate of melting and evaporation, criteria are needed to determine the solid-liquid and liquid-vapor interfaces. Both the profile of the number of atoms [3] and the radial

Fig. 10   Velocity distributions at different z locations at 20 ps. Solid line: Maxwellian distribution; dots: MD simulation.

distribution function [17,18] can be used to determine the locations of the interfaces. For solid argon, the average number density of atoms is 2.52×10^{28} m^{-3} with a spatial distribution shown in Fig. 6. Owing to the lattice structure, the number density of atoms is higher than the average value near the atomic layer and lower between layers. In this work, if the number density of atoms is higher than 2.52×10^{28} m^{-3}, the material is treated as solid. At the front of the melted region, the number density of atoms decreases sharply to less than 8.42×10^{27} m^{-3}, which is about one third of the number density of solid. Therefore, the material is assumed to be vapor at a number density lower than 8.42×10^{27} m^{-3}. Although the criterion used here for the liquid-vapor interface is not quite rigorous due to the large transition region from liquid to vapor, further studies on the liquid-vapor interface using the radial distribution function show that this criterion gives a good approximation of the liquid-vapor interface [16].

Applying these criteria, transient locations of the solid-liquid and liquid-vapor interfaces, as well as the velocities of the interfaces are obtained and are shown in Fig. 9. It is observed that melting and evaporation start at about 10 ps (laser heating starts at around 5 ps). The solid-liquid interface moves into the solid as melting progresses, and the liquid-vapor interface moves outward as the melted region expands because liquid argon is less dense than solid argon. At about 20 ps, both solid-liquid and liquid-vapor interfaces stop moving. The highest velocity of the liquid-vapor interface is about 200 m/s, close to the equilibrium velocity (233.5 m/s) of the argon atom at the boiling temperature. The highest velocity of the solid-liquid interface is about 400 m/s, much smaller than the local sound (longitudinal) speed ($\sim$1275 m/s) in argon [19].

Thermal equilibrium of the system at different z locations is investigated by comparing the velocity distribution with the Maxwellian distribution. Figure 10 shows the comparison at 20 ps. It can be seen that in solid ($z=7.67$ nm), the transient region ($z=10.38$ nm), liquid ($z=12.18$), and vapor ($z=15.79$ nm), the thermal equilibrium is preserved. This is also true at other times, except in vapor in the early stage of ablation when only very few atoms are evaporated.

The existence of thermal equilibrium justifies the use of temperature to discuss the energy transfer process. Temperature distributions at different times are shown in Fig. 11. At 5 ps, laser heating just starts, and the target has a spatially uniform temperature of about 50 K. Note that the initial size of the target extends from 4.5 nm to 12.6 nm. Melting starts at 10 ps as indicated in Fig. 11, and it is clear that at this moment, the temperature is higher than the melting and the boiling point in the heated region, and is even close to the critical point. At 15 ps, a flat region in the temperature distribution is observed around the location of 10 nm, which is the melting interface region. The temperature in this flat region is around 90 K, which is higher than the melting point (83.8 K), indicating superheating at the melting front. Furthermore, superheating is observed at the liquid-vapor interface ($z \sim 13.5$ nm) at 15 ps, which is indicated by the much higher local temperature ($\sim$130 K) compared with the boiling temperature of argon (87.3 K).

An interesting phenomenon is observed at 20 ps, shortly after melting stops. At this moment, a local minimum of temperature is observed at 9.5 nm, which is in the solid-liquid transition region. The temperature is only 60 K, lower than the melting temperature at 1 atm. This minimum temperature disappears gradually due to heat transfer from the surrounding higher temperature regions. This low temperature is likely due to the tensile stress developed in that region. The stress can be calculated as the summation of forces exerted by atoms from both sides of a cross-section of interest, and then divided by the area. The evolution of the stress at the location of 9.5 nm is plotted in Fig. 12, which shows a peak tensile stress at 20 ps, the moment when the minimum temperature appears. A reduced pressure or a tensile stress in argon reduces the melting point [20], therefore causing a temperature

drop. A detailed study of this temperature drop and the coupling between the thermal energy and the mechanical energy is going to be reported elsewhere [16]. It is worth noting that many phase change phenomena obtained in this MD simulation such as the lack of a sharp solid-liquid interface and the temperature variation in liquid could not be predicted using the continuum approach.

The average atomic velocity in the z direction at different times is shown in Fig. 13. At 10 ps, melting just starts, and the average velocity of atoms is close to zero except those on the surface, which have a higher kinetic energy due to the free boundary condition. At 15 ps, velocities are much higher. At the vapor front where the thermal equilibrium is still preserved, the velocity is about 450 m/s, while at locations near the surface, the vapor velocity is much smaller. At 30 ps, non-zero velocities are only observed at locations of 15 nm or further, showing weak evaporation on the liquid surface after laser heating stops. The negative velocity close to the bottom of the target is induced by the momentum conservation of the whole system.

The thickness of the melted and vaporized layer and the rate of phase change are shown in Fig. 14. It is seen that the melting depth is much larger than the vaporization depth. From Fig. 14(b) it is found that melting happens mostly between 10 and 20 ps, while evaporation goes on until 25 ps, and then reduces to a lower level corresponding to the evaporation of liquid in vacuum. The depths of ablation induced by different laser fluences are shown in Fig. 15, which shows a sudden increase of the ablation depth at the laser fluence of 0.5 J/m^2. The laser fluence when substantial ablation occurs is commonly called the threshold fluence of abla-
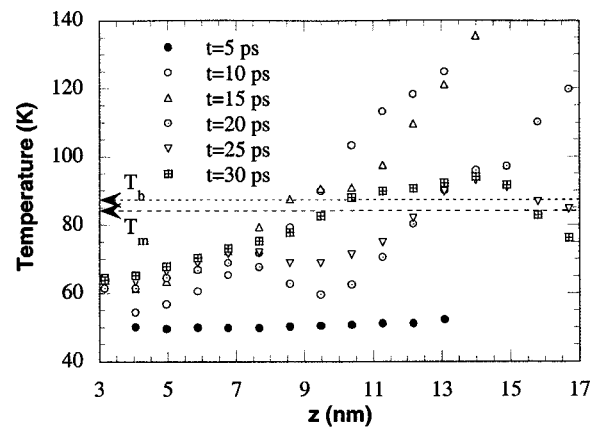

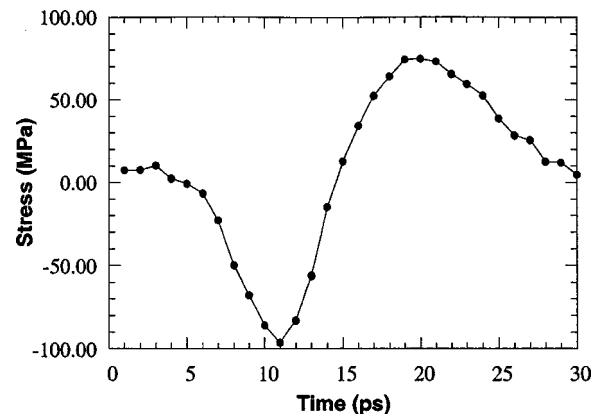**Fig. 11 Temperature distribution in argon illuminated with a laser pulse of 0.7 J/m^2.**

Fig. 12 The stress evolution at the location of 9.5 nm in argon illuminated with a laser pulse of 0.7 J/m^2.
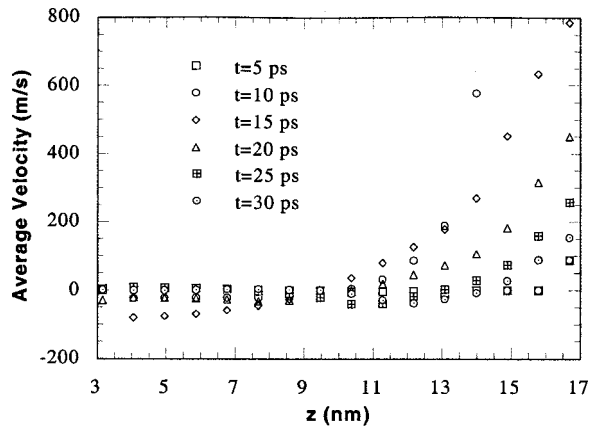
Fig. 13 Spatial distribution of the average velocity in the z direction in argon illuminated with a laser pulse of 0.7 J/m².
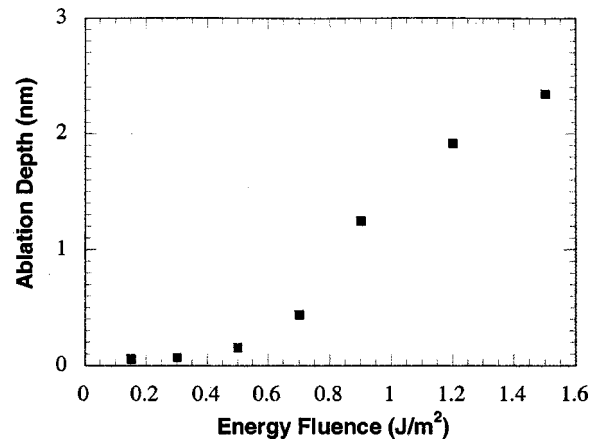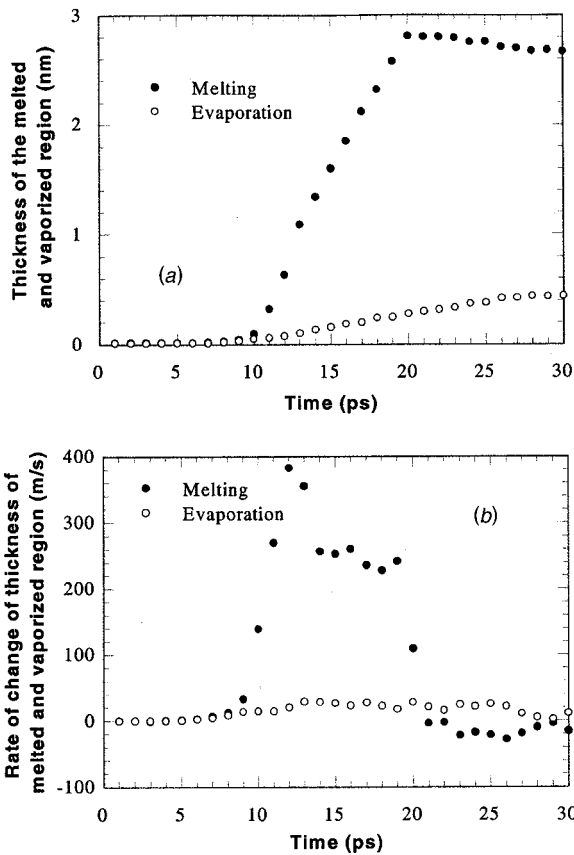

Fig. 14 (a) Thickness of the melted and vaporized solid, and (b) the rate of change in argon illuminated with a laser pulse of 0.7 J/m².

tion. Thus, the calculation shows that with the parameters used in this work, the ablation threshold fluence is 0.5 J/m².

Conclusion

In this work, laser material interaction is studied using MD simulations. It is found that during picosecond laser heating, the heat transfer process predicted using the continuum approach agrees with the result of the MD simulation. When phase change occurs, thermal equilibrium is found in solid, liquid, and vapor phases, and the solid-liquid and liquid-vapor interfaces are superheated. A transition region of about 1 nm, instead of a clear inter-

Fig. 15 The ablation depth induced by different laser fluences in argon.

face is found between the solid and the liquid. At a laser fluence of 0.7 J/m², the solid-liquid interface moves at almost a constant velocity much lower than the local sound speed, while the liquid-vapor interface moves with a velocity close to the local equilibrium velocity. The laser-ablated material burst out of the target with a vapor front velocity of about hundreds of meters per second.

Nomenclature

F = force
I = laser intensity
k = thermal conductivity
k_B = Boltzmann's constant
m = atomic mass
P_M = probability for atoms moving with a velocity v
r = atomic position
r_c = cut off distance
r_s = the nearest neighbor distance
t = time
t_T = preset time constant in velocity scaling
δt = time step
T = temperature
v = velocity
x = coordinate in x-direction
y = coordinate in y-direction
z = coordinate in z-direction

Greek Symbols

χ = velocity scaling factor
ε = LJ well depth parameter
ϕ = potential
σ = equilibrium separation parameter
ξ = current kinetic temperature in velocity scaling

Subscripts

i = index of atoms

References

[1] Shibahara, M., and Kotake, S., 1997, "Quantum Molecular Dynamics Study on Light-to-Heat Absorption Mechanism: Two Metallic Atom System," Int. J. Heat Mass Transf., **40**, pp. 3209–3222.
[2] Shibahara, M., and Kotake, S., 1998, "Quantum Molecular Dynamics Study of Light-to-Heat Absorption Mechanism in Atomic Systems," Int. J. Heat Mass Transf., **41**, pp. 839–849.
[3] Häkkinen, H., and Landman, U., 1993, "Superheating, Melting, and Annealing of Copper Surfaces," Phys. Rev. Lett., **71**, pp. 1023–1026.
[4] Anisimov, S. I., Kapeliovich, B. L., and Perel'man, T. L., 1974, "Electron

Emission From Metal Surfaces Exposed to Ultra-short Laser Pulses,'' Sov. Phys. JETP, **39**, pp. 375–377.

[5] Kotake, S., and Kuroki, M., 1993, ''Molecular Dynamics Study of Solid Melting and Vaporization by Laser Irradiation,'' Int. J. Heat Mass Transf., **36**, pp. 2061–2067.

[6] Herrmann, R. F. W., and Campbell, E. E. B., 1998, ''Ultrashort Pulse Laser Ablation of Silicon: an MD Simulation Study,'' Applied Physics A, **66**, pp. 35–42.

[7] Zhigilei, L. V., Kodali, P. B. S., and Garrison, J., 1997, ''Molecular Dynamics Model for Laser Ablation and Desorption of Organic Solids,'' J. Phys. Chem. B, **101**, pp. 2028–2037.

[8] Zhigilei, L. V., Kodali, P. B. S., and Garrison, J., 1998, ''A Microscopic View of Laser Ablation,'' J. Phys. Chem. B, **102**, pp. 2845–2853.

[9] Ohmura, E., Fukumoto, I., and Miyamoto, I., 1999, ''Modified Molecular Dynamics Simulation on Ultrafast Laser Ablation of Metal,'' *Proceedings of the International Congress on Applications of Lasers and Electro-Optics*, Laser Institute of America, Orlando, pp. 219–228.

[10] Girifalco, L. A. and Weizer, V. G., 1959, ''Application of the Morse Potential Function to Cubic Metals,'' Phys. Rev., **114**, pp. 687–690.

[11] Etcheverry, J. I., and Mesaros, M., 1999, ''Molecular Dynamics Simulation of the Production of Acoustic Waves by Pulsed Laser Irradiation,'' Phys. Rev. B, **60**, pp. 9430–9434.

[12] Allen, M. P., and Tildesley, D. J., 1987, *Computer Simulation of Liquids*, Clarendon Press, Oxford.

[13] Broughton, J. Q., and Gilmer, G. H., 1983, ''Molecular Dynamics Investigation of the Crystal-Fluid Interface. I. Bulk Properties,'' J. Chem. Phys., **79**, pp. 5095–5104.

[14] Berendsen, H. J. C., Postma, J. P. M., van Gunsteren, W. F., DiNola, A., and Haak, J. R., 1984, ''Molecular Dynamics With Coupling to an External Bath,'' J. Chem. Phys., **81**, pp. 3684–90.

[15] Peterson, O. G., Batchelder, D. N., and Simmons, R. O., 1966, ''Measurements of X-Ray Lattice Constant, Thermal Expansivity, and Isothermal Compressibility of Argon Crystals,'' Phys. Rev., **150**, pp. 703–711.

[16] Wang, X., and Xu, X., 2001, ''Molecular Dynamics Simulation of Thermal and Thermomechanical Phenomena in Picosecond Laser Material Interaction,'' submitted to the 12th International Heat Transfer Conference.

[17] Wang, X., 2001, ''Thermal and Thermomechanical Phenomena in Laser Material Interaction,'' Ph.D. thesis, Purdue University, West Lafayette, IN.

[18] Chokappa, D. K., Cook, S. J., and Clancy, P., 1989, ''Nonequilibrium Simulation Method for the Study of Directed Thermal Processing,'' Phys. Rev. B, **39**, pp. 10075–10087.

[19] Keeler, G. J., and Batchelder, D. N., 1970, ''Measurement of the Elastic Constants of Argon from 3 to 77°K,'' J. Phys. C, **3**, pp. 510–522.

[20] Ishizaki, K., Spain, I. L., and Bolsaitis, R., 1975, ''Measurements of Longitudinal and Transverse Ultrasonic Wave Velocities in Compressed Solidified Argon and Their Relationship to Melting Theory,'' J. Chem. Phys., **63**, pp. 1401–1410.